

Gravitational Anomaly Measurement in Wide Binaries is Sensitive to Orbital Modeling

SERAT M. SAAD¹ AND YUAN-SEN TING^{1,2,3}

¹*Department of Astronomy, The Ohio State University, Columbus, OH 43210, USA*

²*Center for Cosmology and AstroParticle Physics (CCAPP), The Ohio State University, Columbus, OH 43210, USA*

³*Max-Planck-Institut für Astronomie, Königstuhl 17, D-69117 Heidelberg, Germany*

ABSTRACT

Recent work by [Chae et al. \(2026\)](#) reported a gravitational anomaly in 36 wide-binary pairs, finding a gravity boost factor of $\gamma \equiv G_{\text{eff}}/G_{\text{N}} \approx 1.60_{-0.14}^{+0.17}$ at low accelerations, consistent with predictions from Modified Newtonian Dynamics (MOND). We reanalyze the same dataset using a hierarchical Bayesian model that infers a global γ across all systems while fitting three-dimensional orbital elements. Our model yields $\gamma = 1.12_{-0.22}^{+0.27}$, consistent with Newtonian gravity ($\gamma = 1$) at the $\sim 0.4\sigma$ level. To identify the source of the discrepancy, we perform a test using an approach similar to [Chae et al. \(2026\)](#), replacing the semi-major axis with a geometric de-projection of the observed projected separation. This test yields $\gamma = 1.56_{-0.18}^{+0.21}$, closely matching the result of [Chae et al. \(2026\)](#). This suggests that the inferred value of γ is sensitive to how the three-dimensional orbital separation is modeled, and including an independent semi-major axis parameter can account for velocity excesses that would otherwise be attributed to non-Newtonian gravity.

Keywords: gravitation — methods: statistical — techniques: radial velocities — binaries: visual — stars: kinematics and dynamics

1. INTRODUCTION

Testing gravity in the low-acceleration regime is an ongoing challenge in astrophysics. On galactic scales, the observational predictions deviate from Newtonian predictions based on visible matter alone ([Zwicky 1937](#); [Rubin & Ford 1970](#); [Sofue & Rubin 2001](#)). The standard Λ CDM cosmological model accounts for these deviations by invoking cold dark matter (CDM) ([Springel et al. 2005](#); [Eisenstein et al. 2005](#)). The Λ CDM model has been successful at explaining large-scale structure and the cosmic microwave background ([Planck Collaboration et al. 2020a,b](#)). An alternative approach, Modified Newtonian Dynamics (MOND), was proposed by Mordehai Milgrom in 1983 ([Milgrom 1983](#)). MOND suggests that gravity is modified below an acceleration scale $a_0 \approx 1.2 \times 10^{-10} \text{ m s}^{-2}$ ([Milgrom 1983](#)). MOND has been successful in reproducing galaxy rotation curves and scaling relations ([Sanders & McGaugh 2002](#); [Famaey & McGaugh 2012](#); [McGaugh 2016](#); [Lelli et al. 2016](#)), but faces challenges on cluster and cosmological scales ([Sanders 2003](#); [Angus 2008](#)). Distinguishing between these two frameworks requires tests in environments where their predictions differ and the systematic uncertainties can be controlled.

Wide-binary stars, separated by thousands of AU, provide one such environment where gravity can be tested. At these separations, the internal gravitational acceleration of the binary can be compared to the MOND acceleration scale a_0 . MOND framework therefore predicts deviation from Newtonian gravity in these systems. Testing MOND with wide binaries requires careful consideration of several theoretical ingredients. In MOND, the transition from Newtonian to modified gravity is governed by an interpolating function $\mu(x)$ where $x = a/a_0$, with $\mu \rightarrow 1$ for $x \gg 1$ (Newtonian regime) and $\mu \rightarrow x$ for $x \ll 1$ (deep-MOND regime). The exact form of μ is not uniquely specified by the theory, and different choices lead to different predicted gravity enhancements at intermediate accelerations ([Famaey & McGaugh 2012](#)). Furthermore, wide binaries in the solar neighborhood are subject to the external field effect (EFE): the external gravitational acceleration from the Galaxy, $a_{\text{ext}} \approx 1.8 \times 10^{-10} \text{ m s}^{-2}$ at the solar position, is comparable to a_0 and much larger than the internal acceleration of the binary. In MOND, the EFE can suppress the internal anomaly, so the predicted gravity boost depends on a_{ext}/a_0 as well as on the interpolating function and the specific MOND formulation ([Banik & Zhao 2018](#); [Chae et al. 2022](#)).

However, the gravity boost factor $\gamma \equiv G_{\text{eff}}/G_{\text{N}}$, defined as the ratio of the effective gravitational constant to the Newtonian value, can be measured independently of these theoretical choices. The inference of γ is a kinematic measurement that assumes only Keplerian orbits; it does not assume any particular value of a_0 , any specific interpolating function, or any MOND framework. Previous wide-binary studies using *Gaia* data have taken this approach, reporting $\gamma = 1.43 \pm 0.06$ (Chae 2023), $\gamma = 1.49 \pm 0.2$ (Chae 2024), $\gamma = 1.5 \pm 0.2$ (Hernandez et al. 2024), and most recently $\gamma = 1.6 \pm 0.2$ (Chae et al. 2026), which can be compared to AQUAL predictions of $\gamma \approx 1.4$ for wide binaries in the EFE-dominated regime of the solar neighborhood (Banik & Zhao 2018; Chae et al. 2022). In contrast, Banik et al. (2024) reported preference for Newtonian gravity ($\gamma = 1$). The conflicting conclusions highlight that the result may be sensitive to the statistical methodology or the data used for the analysis.

Recent work has introduced high-precision radial velocities (RVs) to enable three-dimensional analysis of wide-binary orbits. Saglia et al. (2025) obtained RVs for 32 wide binaries and found results broadly consistent with Newtonian gravity. Chae (2025b) reanalyzed the same sample and reported a tentative gravitational anomaly of $\gamma \equiv G_{\text{eff}}/G_{\text{N}} \approx 1.60_{-0.14}^{+0.17}$ for systems with low internal accelerations. Most recently, Chae et al. (2026) assembled a sample of 36 wide binaries with high-precision 3D velocities and reported $\gamma \approx 1.6 \pm 0.2$, claiming a $> 3\sigma$ detection of deviation from Newtonian gravity. The methodology used by Chae et al. (2026) and Chae (2025b) consists of two steps: first, for each binary system, a Bayesian inference is performed to derive a posterior distribution of Γ , where $\Gamma = \log_{10} \sqrt{\gamma}$ along with nuisance orbital parameters; second, the per-system posteriors are statistically consolidated to derive a combined Γ . While this approach has merit, aspects of the model formulation, particularly the treatment of projected separation and the absence of an independent semi-major axis parameter, may influence the inferred γ .

In our previous work (Mahmud Saad & Ting 2025, hereafter S&T25), we developed a hierarchical Bayesian framework for testing MOND with wide-binary kinematics and applied that to the wide binaries from the C3PO survey (Yong et al. 2023). That model fit three-dimensional orbital elements for all systems while inferring a global MOND acceleration scale a_0 . The framework included the MOND interpolating function and an analytic treatment of the EFE, and tested two interpolating functions ($b = 1$ and $b = 2$). The C3PO systems were found to reside in the MOND transition regime,

and the analysis yielded tension with the canonical a_0 value at $\sim 3\sigma$ ($b = 1$) and $\sim 2\sigma$ ($b = 2$). Although, because the C3PO test was performed in the transition regime, the results were sensitive to the choice of interpolating function and the EFE treatment.

In this paper, we adapt the framework of S&T25 to infer the gravity boost factor γ for 36 wide binaries from Chae et al. (2026). In Section 2, we describe the dataset from Chae et al. (2026). In Section 3, we present our hierarchical Bayesian model. In Section 4, we report the results of our two model variants, discuss the interpretation of these results, and place our findings in the context of previous wide-binary gravity tests.

2. DATA

We use the sample of 36 wide-binary systems assembled by Chae et al. (2026). This sample was constructed through selection criteria designed to identify gravitationally bound pairs with 3D kinematics: multi-epoch RV verification, speckle interferometry to exclude unresolved tertiary companions, Hipparcos-*Gaia* proper motion consistency checks, and *Gaia* RUWE < 1.4 .

The RVs come from multiple instruments: the Las Cumbres Observatory (LCO) Network of Robotic Echelle Spectrographs (NRES), the Gemini-North MAROON-X spectrograph (MAROON-X), the High Accuracy Radial velocity Planet Searcher (HARPS) spectrograph on the European Southern Observatory (ESO) 3.6m telescope (Saglia et al. 2025), and the Apache Point Observatory Galactic Evolution Experiment (APOGEE) from Sloan Digital Sky Survey (SDSS) Data Release 17 (DR17) (Abdurro'uf et al. 2022). The RV precisions vary across instruments, with HARPS providing the highest precision ($\sim 1\text{--}5 \text{ m s}^{-1}$) and LCO/NRES providing precisions of $\sim 50\text{--}300 \text{ m s}^{-1}$.

For each system, we use the following observational quantities: (i) the positions of both components from *Gaia* DR3, from which we compute the projected separation; (ii) the proper motions and their uncertainties from *Gaia* DR3, from which we compute differential proper motions $\Delta\mu_\alpha$ and $\Delta\mu_\delta$; (iii) the RV difference between the two components and its uncertainty, as reported by Chae et al. (2026); and (iv) stellar masses. For stellar masses, we use *Gaia* FLAME estimates where available (Sacco et al. 2014), supplemented by the mass estimates from Chae (2023) for systems lacking FLAME values. Unlike our previous analysis in S&T25, which used differential RVs measured from the same spectrograph in a single epoch, the RVs in the Chae et al. (2026) sample are absolute RVs measured independently for each star, often from different instruments and epochs. The RV difference $\Delta v_r = v_{r,B} - v_{r,A}$ is computed from

these absolute measurements. All observational data are taken directly from [Chae et al. \(2026\)](#) and are available in the appendix of the paper.

3. METHODS

Our model follows the hierarchical Bayesian framework developed in [S&T25](#), with the key difference that we replace the MOND interpolating function and acceleration scale a_0 with a global gravity boost factor γ , defined such that $G_{\text{eff}} = \gamma \cdot G_{\text{N}}$. Newtonian gravity corresponds to $\gamma = 1$, while MOND predictions for wide binaries in the solar neighborhood give $\gamma \approx 1.4$ – 1.6 ([Banik & Zhao 2018](#); [Chae et al. 2022, 2026](#)). The quantity $\Gamma = \log_{10} \sqrt{\gamma}$ used by [Chae et al. \(2026\)](#) is related by $\gamma = 10^{2\Gamma}$, with $\Gamma = 0$ corresponding to Newtonian.

We model each wide binary as a two-body Keplerian system with six orbital elements: semi-major axis a , eccentricity e , inclination i , longitude of ascending node Ω , argument of periastron ω , and mean anomaly M . The orbital velocity depends on γ through

$$v = \sqrt{\frac{\gamma G_{\text{N}} M_{\text{tot}}}{r}} \cdot F \quad (1)$$

where r is the instantaneous separation, $F = (1 + e^2 + 2e \cos \nu)/(1 + e \cos \nu)$ is the velocity variation with orbital phase, and M_{tot} is the total mass. The orbital-frame positions and velocities are rotated into the ICRS frame to produce model-predicted observables (r_{\perp} , Δv_r , $\Delta \mu_{\alpha}$, $\Delta \mu_{\delta}$), following the coordinate transformation described in [S&T25](#).

3.1. Hierarchical Bayesian model

Rather than fitting γ independently for each system and then combining the results as in [Chae et al. \(2026\)](#), we fit a global γ shared across all 36 systems. The graphical model is shown in [Figure 1](#).

The joint posterior is,

$$p(\gamma, \{\theta_j\} | \{d_j\}) \propto p(\gamma) \prod_{j=1}^N p(d_j | \gamma, \theta_j) p(\theta_j) \quad (2)$$

where the per-system parameters,

$$\theta_j = \{a_j, e_j, i_j, \Omega_j, \omega_j, \phi_j, M_{1,j}, M_{2,j}\}$$

and, the observables,

$$d_j = \{r_{\perp,j}, \Delta v_{r,j}, \Delta \mu_{\alpha,j}, \Delta \mu_{\delta,j}\}$$

We adopt priors following [S&T25](#) with minor modifications. We place a uniform prior, $\Gamma \sim \mathcal{U}(-1, 1)$, where $\Gamma = \log_{10} \sqrt{\gamma}$ and γ is the gravity boost factor. For masses, we use Gaussian priors centered

on the *Gaia* FLAME or [Chae \(2023\)](#) estimates. For angular elements, we assign isotropic priors ($\cos i \sim \mathcal{U}(-1, 1)$; $\omega, \Omega, \phi \sim \mathcal{U}(0, 2\pi)$), and for eccentricity, we use separation-dependent thermal distribution of [Hwang et al. \(2022\)](#) as described in [S&T25](#).

The prior on the semi-major axis is important to this analysis. We parameterize $a = r_{\perp} \times \exp(\eta)$, where r_{\perp} is the observed projected separation and $\eta = \ln(a/r_{\perp})$ is a free parameter for each system. We place a normal prior on η whose mean depends on the eccentricity of the same system,

$$\eta \sim \mathcal{N}(\mu_e, \sigma_a^2), \quad \mu_e = \sqrt{1 - e^2} - \ln\left(1 + \sqrt{1 - e^2}\right), \quad (3)$$

with $\sigma_a = 0.6$. The center μ_e is derived from the statistical relationship between the semi-major axis and the projected separation for a binary observed at a random orbital phase and viewing angle. We present the derivation in [Appendix A](#).

The likelihood follows [S&T25](#). Each system contributes three terms:

$$r_{\perp,\text{obs}} \sim \mathcal{N}(r_{\perp,\text{model}}, \sigma_r^2) \quad (4)$$

$$\Delta v_{r,\text{obs}} \sim t_5(\Delta v_{r,\text{model}}, \sigma_{\Delta v_r}^2 + \sigma_{\text{jitter}}^2) \quad (5)$$

$$\Delta \mu_{\text{obs}} \sim \mathcal{N}(\Delta \mu_{\text{model}}, \sigma_{\mu}^2 + \sigma_{\text{pm,jit}}^2) \quad (6)$$

where t_5 denotes a Student- t distribution with five degrees of freedom, used for the RV likelihood to provide robustness against outliers. The parameters σ_{jitter} and $\sigma_{\text{pm,jit}}$ are global nuisance parameters with half-normal priors. We perform inference using Hamiltonian Monte Carlo (HMC) with the No-U-Turn Sampler (NUTS) ([Hoffman et al. 2014](#)), implemented in PyMC ([Salvatier et al. 2015](#)), following the same approach as [S&T25](#). We run 4 chains, each with 2000 tuning steps and 3000 sampling steps, with a target acceptance probability of 0.98.

3.2. Using two different models

We consider two model variants that differ in how the three-dimensional separation is determined:

For the baseline model, the semi-major axis a is a free parameter, and the instantaneous separation r_{true} is computed from a , e , and the true anomaly ν through Kepler's equation, as described in [S&T25](#). The projected separation r_{\perp} enters the likelihood as an observable with Gaussian uncertainty. This allows the model to infer an orbital scale independent of the observed projected separation.

We also consider a geometric de-projection model. In this variant, we replace the semi-major axis parameter with a geometric de-projection of the observed projected

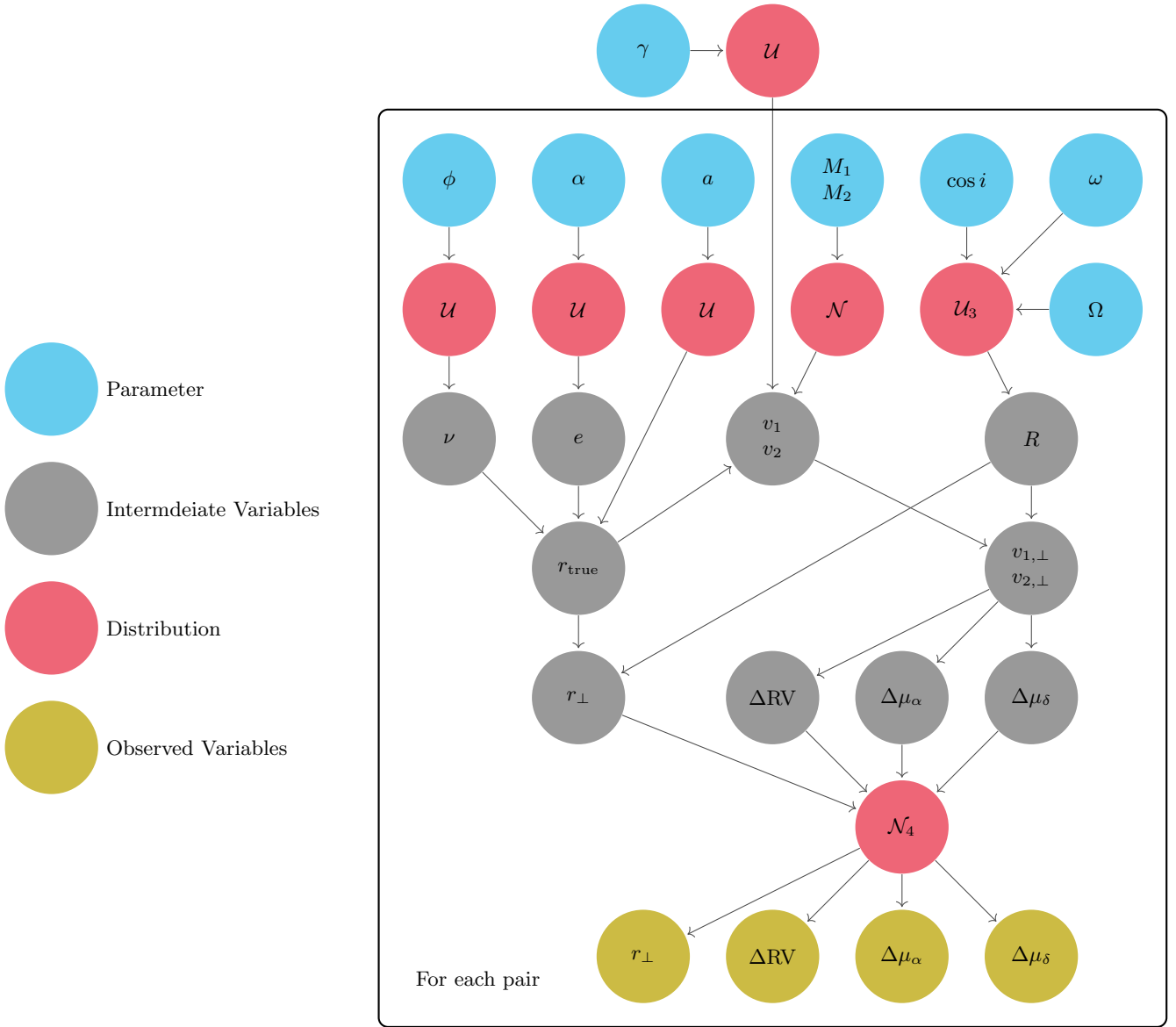


Figure 1. Graphical representation of the hierarchical Bayesian model for inferring the gravity boost factor γ . The global parameter γ (blue) is shared across all binary systems. The plate notation indicates that the enclosed structure is replicated for each of the $N = 36$ systems. For each system, we infer six orbital elements ($a, \alpha, \phi, i, \omega, \Omega$) and masses (M_1, M_2). These determine intermediate quantities (gray): true anomaly ν , true separation r_{true} , rotation matrix R , and component velocities v_1, v_2 . The model predicts four observables (yellow): projected separation r_{\perp} , RV difference Δv_r , and differential proper motions $\Delta\mu_{\alpha}, \Delta\mu_{\delta}$. Red nodes denote probability distributions.

separation, following the approach of [Chae et al. \(2026\)](#). The true separation is derived as,

$$r_{\text{true}} = \frac{r_{\perp}}{\sqrt{\cos^2 \phi + \cos^2 i \sin^2 \phi}} \quad (7)$$

where ϕ is the orbital position angle and i is the inclination. This couples the three-dimensional orbital scale directly to the observed r_{\perp} and does not allow for an independent determination of a . All other aspects of the model remain identical to the baseline.

4. RESULTS & IMPLICATIONS

4.1. Results

The results of both model variants are summarized in [Table 1](#) and [Figure 2](#). For the baseline model, our hierarchical Bayesian analysis yields $\gamma = 1.12$ with a 68% credible interval of $[0.90, 1.38]$ and a 95% credible interval of $[0.74, 1.72]$. The Newtonian value $\gamma = 1$ is well within the 68% credible interval. The probability that $\gamma > 1$ is 0.70. In the notation of [Chae et al. \(2026\)](#), this corresponds to $\Gamma = \log_{10} \sqrt{\gamma} \approx 0.02$.

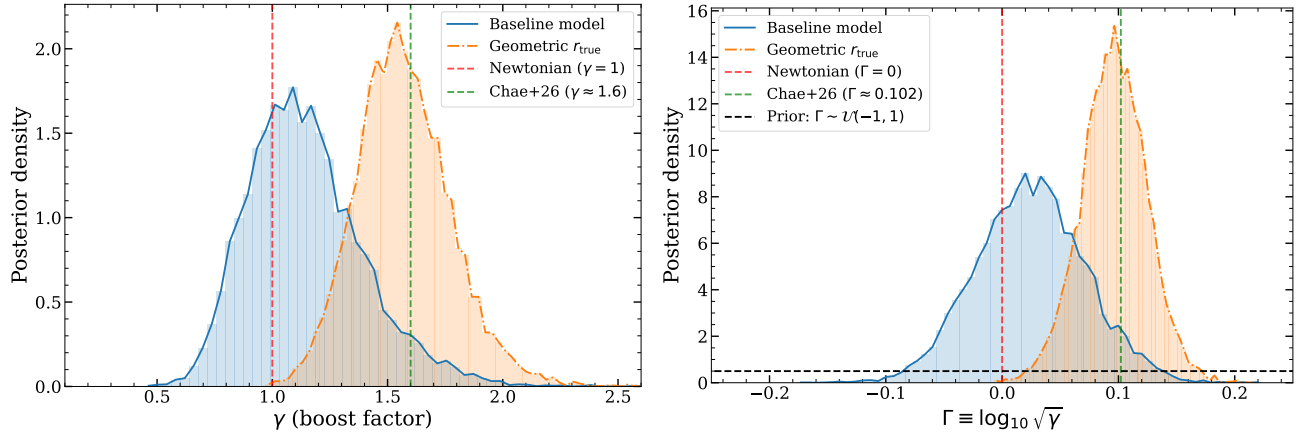


Figure 2. Posterior distributions for the gravitational boost parameter. *Left:* posterior distributions of γ for the two model variants. The blue solid curve shows the baseline model ($\gamma = 1.12$), which includes an independent semi-major axis parameter. The orange dashed curve shows the geometric de-projection model ($\gamma = 1.56$), in which r_{true} is derived directly from the observed projected separation. The vertical red dashed line marks the Newtonian prediction ($\gamma = 1$), while the vertical green dashed line indicates $\gamma \approx 1.6$ reported by Chae et al. (2026). *Right:* the same posteriors expressed in terms of $\Gamma \equiv \log_{10} \sqrt{\gamma}$. The horizontal dotted line shows the flat prior $\Gamma \sim \mathcal{U}(-1, 1)$ used in the inference. The two models differ only in the treatment of the orbital separation, yet the inferred gravitational boost shifts substantially.

Table 1. Model Comparison Results

| Model | γ | 68% CI | $P(\gamma > 1)$ |
|-----------------------------|----------|--------------|-----------------|
| Baseline | 1.12 | [0.90, 1.38] | 0.70 |
| Geometric r_{true} | 1.56 | [1.38, 1.77] | 1.00 |

NOTE—The baseline model includes an independent semi-major axis parameter with an eccentricity-dependent prior (Equation 3). The geometric r_{true} model replaces it with a de-projection of the observed projected separation, analogous to the approach of Chae et al. (2026). The Chae et al. (2026) result is $\gamma \approx 1.60^{+0.17}_{-0.14}$. The median posterior γ , 68% credible interval, and posterior probability of a gravity enhancement $P(\gamma > 1)$ are listed for each model.

Replacing the semi-major axis with the geometric de-projection shifts the posterior to $\gamma = 1.56$ with a 68% credible interval of [1.38, 1.77] and a 95% credible interval of [1.20, 2.01]. The probability that $\gamma > 1$ is effectively unity. This result is consistent with the Chae et al. (2026) value of $\gamma \approx 1.60^{+0.17}_{-0.14}$.

The two models are identical in every respect except the treatment of the three-dimensional separation, yet the inferred γ differs by $\Delta\gamma \approx 0.44$, shifting from a result consistent with Newtonian gravity to one consistent with the reported gravitational anomaly. Figure 3 summarizes the point at which the two models diverge and how that difference propagates to the inferred value of γ .

4.2. The role of the semi-major axis

In the two different models we used, we parametrize the orbital scale differently. In the baseline model, a is treated as an independent parameter. The instantaneous separation is then computed from,

$$r_{\text{true}} = \frac{a(1 - e^2)}{1 + e \cos \nu} \quad (8)$$

and the projected separation is obtained by projecting the orbit onto the plane of the sky. The observed r_{\perp} enters through the likelihood, so the model asks whether a given orbit predicts a projected separation consistent with the data. In the geometric de-projection model, the observed projected separation is used to define the instantaneous three-dimensional separation (Equation 7). The semi-major axis is not used in this parametrization, but it can be obtained from,

$$a = r_{\text{true}} \frac{1 + e \cos \nu}{1 - e^2} \quad (9)$$

In this case, a is not an independent parameter. The orbital scale is tied directly to the observed projected separation and the orbital geometry.

The two models therefore use the same Keplerian relations but place the projected separation at different points in the inference. In the baseline model, r_{\perp} is a predicted observable. In the geometric model, r_{\perp} is used to define part of the orbit itself. This changes the set of allowed combinations of r_{true} , a , and γ .

This difference matters because the velocity depends on both r_{true} and a . In the geometric model, once r_{\perp} , i , ϕ , e , and ν are specified, the corresponding values of

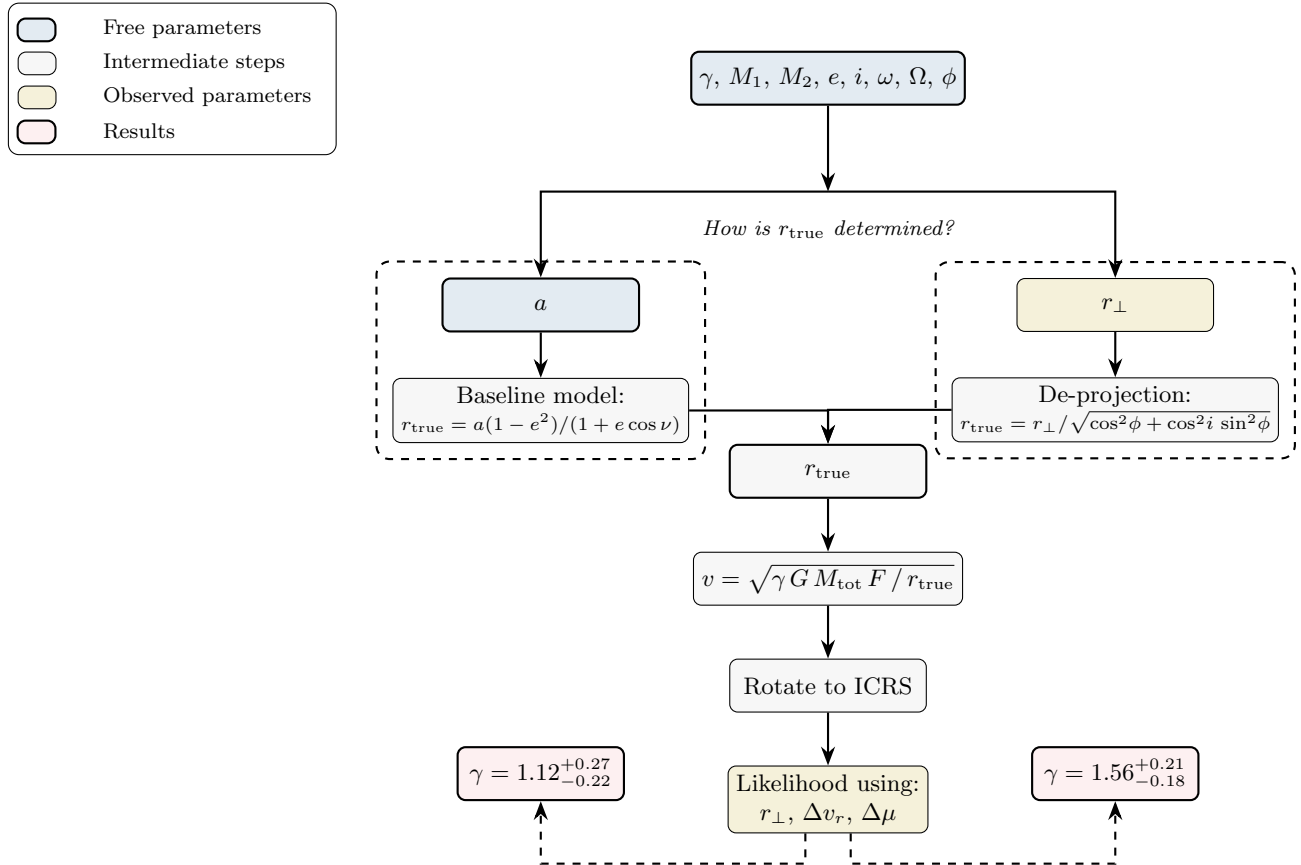


Figure 3. Diagram showing how the two model variants diverge in their determination of the three-dimensional separation r_{true} , while sharing all other components. At the branch point, baseline model treats the semi-major axis a as a free parameter and computes r_{true} from Kepler’s equation, yielding $\gamma = 1.12^{+0.27}_{-0.22}$, consistent with Newtonian gravity. Geometric model derives r_{true} directly from the observed projected separation r_{\perp} through geometric de-projection, yielding $\gamma = 1.56^{+0.21}_{-0.18}$, consistent with the anomaly reported by [Chae et al. \(2026\)](#). All other steps, like velocity computation, coordinate rotation, and comparison to observables are identical between the two models.

r_{true} and a are fixed. In the baseline model, the sampler can explore a wider range of orbital scales while still requiring the predicted r_{\perp} to agree with the data. The same observed system can therefore be assigned different posterior support in the two parameterizations.

In our analysis, this leads to different inferences for γ . When a is treated as an independent parameter, we obtain $\gamma = 1.12^{+0.27}_{-0.22}$, which is consistent with Newtonian gravity. When the orbital scale is set by geometric de-projection of the observed projected separation, we obtain $\gamma = 1.56^{+0.21}_{-0.18}$, consistent with [Chae et al. \(2026\)](#). This comparison shows that for the present dataset, the inferred value of γ is sensitive to how the orbital scale is introduced into the model.

4.3. Additional methodological differences

Beyond the semi-major axis treatment, several other differences exist between our approach and that of [Chae et al. \(2026\)](#) that may contribute at a smaller level.

Firstly, we use NUTS/HMC in PyMC, which explores high-dimensional correlated posteriors efficiently, while [Chae et al. \(2026\)](#) uses emcee with 200 walkers. For a six-parameter per-system model, emcee is adequate, and this difference is unlikely to drive the discrepancy in the inferred γ .

Secondly, we use a hierarchical model where γ is a global parameter fit jointly across all systems, whereas [Chae et al. \(2026\)](#) fits Γ for each system independently and consolidates the per-system posteriors using the method of [Hill & Miller \(2011\)](#). Both approaches weight systems by how well their orbits are constrained: in a hierarchical framework this happens automatically through the joint likelihood, while in the [Chae et al. \(2026\)](#) approach the consolidation step accounts for per-system posterior widths. This difference is also unlikely to be the primary driver of the discrepancy.

Thirdly, the treatment of the projected separation may also play a role. In our baseline model, r_{\perp} enters as an observable with Gaussian uncertainty, so that

any error in r_{\perp} is propagated into the posterior on γ . In the [Chae et al. \(2026\)](#) model, r_{\perp} is treated as a fixed quantity. Since $v^2 \propto \gamma/r$, an underestimated separation could contribute to an overestimated γ . To test whether this treatment matters in practice, we run an additional variant of the geometric de-projection model in which r_{\perp} is treated as exact and the r_{\perp} likelihood term is removed. This yields $\gamma = 1.59_{-0.19}^{+0.23}$, nearly identical to the geometric model with r_{\perp} likelihood included ($\gamma = 1.56_{-0.18}^{+0.21}$). The shift of $\Delta\gamma \approx 0.03$ confirms that the r_{\perp} treatment is subdominant compared to the semi-major axis parameterization. We present this comparison in detail in [Appendix B](#).

4.4. Relation to previous work

Our result is consistent with our previous analysis ([Mahmud Saad & Ting 2025](#)), where we applied a similar hierarchical Bayesian framework to the C3PO wide-binary sample and found the canonical MOND value of $a_0 = 1.2 \times 10^{-10} \text{ m s}^{-2}$ to be excluded at $\sim 3\sigma$ and $\sim 2\sigma$ for two different interpolating functions. The present analysis is more informative because it uses the same data as [Chae et al. \(2026\)](#), who reported a gravitational anomaly in these 36 systems. It also differs from our previous work in that here we estimate γ , which is independent of the choice of interpolating function or EFE treatment.

Our result is also consistent with the findings of [Banik et al. \(2024\)](#) and [Pittordis & Sutherland \(2023\)](#), who used ensemble statistics of *Gaia* proper motions to conclude that Newtonian gravity is preferred. We note that [Saglia et al. \(2025\)](#), who provided many of the HARPS RVs used by [Chae et al. \(2026\)](#), found that Newtonian Keplerian orbits provide adequate fits for most of their systems. Their analysis did not fit for a gravity boost parameter; rather, it demonstrated that the observed kinematics are consistent with Newtonian orbits. The fact that [Chae et al. \(2026\)](#) infers $\gamma > 1$ from overlapping data underscores that the inferred anomaly depends on the modeling framework, consistent with the sensitivity to orbital parameterization that we identify in this work.

5. CONCLUSIONS

We reanalyzed the 36 wide binaries from [Chae et al. \(2026\)](#) using a hierarchical Bayesian model that fits a global gravity boost factor γ while modeling three-dimensional Keplerian orbits for each system. In our baseline model, where the semi-major axis is treated as an independent parameter, we find $\gamma = 1.12_{-0.22}^{+0.27}$, which is consistent with Newtonian gravity. This dif-

fers from the result of [Chae et al. \(2026\)](#), who reported $\gamma \approx 1.60_{-0.14}^{+0.17}$ for the same systems.

To understand this difference, we repeated the analysis with a second model that follows the geometric de-projection approach used by [Chae et al. \(2026\)](#), where the three-dimensional separation is derived directly from the observed projected separation and no independent semi-major axis is included. This model gives $\gamma = 1.56_{-0.18}^{+0.21}$, in close agreement with [Chae et al. \(2026\)](#). This comparison indicates that the inferred value of γ depends strongly on how the orbital scale is introduced into the inference.

Our result suggests that the current evidence for a gravitational anomaly in this 36-system sample is not robust to reasonable changes in orbital modeling. For this dataset, the conclusion about whether γ is consistent with Newtonian gravity depends on the assumed relation between projected separation, true separation, and semi-major axis. More generally, this indicates that wide-binary gravity tests require careful treatment of orbital scale and model assumptions before drawing conclusions about non-Newtonian gravity.

ACKNOWLEDGMENTS

We thank Indranil Banik and Xavier Hernandez for helpful discussions. We also thank Kyu-Hyun Chae for making the data and code publicly available.

SMS is supported by the Distinguished University Fellowship awarded by The Ohio State University. YST is supported by NSF under Grant AST-2406729 and a Humboldt Research Award from the Alexander von Humboldt Foundation.

This work has made use of data from the European Space Agency (ESA) mission *Gaia* (<https://www.cosmos.esa.int/gaia>), processed by the *Gaia* Data Processing and Analysis Consortium (DPAC).

This work has made use of the following software packages: AstroPy ([Astropy Collaboration et al. 2013](#)), PyMC ([Salvatier et al. 2015](#)), and ArviZ ([Kumar et al. 2019](#)). This project has also benefited from collaboration with Cursor and Claude Code for coding development.

DATA & CODE AVAILABILITY

The data underlying this article are available in the published tables and supplementary materials of [Chae et al. \(2026\)](#). The analysis code and derived posterior samples are available on <https://github.com/seratsaad/wb3d-gamma>. The details of the analysis done by [Chae et al. \(2026\)](#) can be found in Zenodo at [Chae \(2025a\)](#).

REFERENCES

- Abdurro'uf et al., 2022, *ApJS*, 259, 35
- Angus G. W., 2008, *MNRAS*, 387, 1481
- Astropy Collaboration et al., 2013, *A&A*, 558, A33
- Banik I., Zhao H., 2018, *MNRAS*, 480, 2660
- Banik I., Pittordis C., Sutherland W., Famaey B., Ibata R., Mieske S., Zhao H., 2024, *MNRAS*, 527, 4573
- Chae K.-H., 2023, *ApJ*, 952, 128
- Chae K.-H., 2024, *ApJ*, 972, 186
- Chae K.-H., 2025a, Bayesian 3D modeling of the orbital dynamics of wide binary stars: General Python algorithms to infer gravity, doi:10.5281/zenodo.17113129
- Chae K.-H., 2025b, arXiv e-prints, p. arXiv:2508.11996
- Chae K.-H., Lelli F., Desmond H., McGaugh S. S., Schombert J. M., 2022, *PhRvD*, 106, 103025
- Chae K.-H., Lee B.-C., Hernandez X., Orlov V. G., Lim D., Turnshek D. A., Lee Y.-W., 2026, arXiv e-prints, p. arXiv:2601.21728
- Eisenstein D. J., et al., 2005, *ApJ*, 633, 560
- Famaey B., McGaugh S. S., 2012, *Living Reviews in Relativity*, 15, 10
- Hernandez X., Verteletskiy V., Nasser L., Aguayo-Ortiz A., 2024, *MNRAS*, 528, 4720
- Hill T. P., Miller J., 2011, *Chaos*, 21, 033102
- Hoffman M. D., Gelman A., et al., 2014, *J. Mach. Learn. Res.*, 15, 1593
- Hwang H.-C., Ting Y.-S., Zakamska N. L., 2022, *MNRAS*, 512, 3383
- Kumar R., Carroll C., Hartikainen A., Martin O., 2019, *The Journal of Open Source Software*, 4, 1143
- Lelli F., McGaugh S. S., Schombert J. M., Pawlowski M. S., 2016, *ApJL*, 827, L19
- Mahmud Saad S., Ting Y.-S., 2025, arXiv e-prints, p. arXiv:2512.19652
- McGaugh S. S., 2016, *ApJL*, 832, L8
- Milgrom M., 1983, *ApJ*, 270, 371
- Pittordis C., Sutherland W., 2023, *The Open Journal of Astrophysics*, 6, 4
- Planck Collaboration et al., 2020a, *A&A*, 641, A1
- Planck Collaboration et al., 2020b, *A&A*, 641, A6
- Rubin V. C., Ford Jr. W. K., 1970, *ApJ*, 159, 379
- Sacco G. G., et al., 2014, *A&A*, 565, A113
- Saglia R., Pasquini L., Patat F., Ludwig H.-G., Giribaldi R., Leao I., de Medeiros J. R., Murphy M. T., 2025, *A&A*, 699, A151
- Salvatier J., Wiecki T., Fonnesbeck C., 2015, arXiv e-prints, p. arXiv:1507.08050
- Sanders R. H., 2003, *MNRAS*, 342, 901
- Sanders R. H., McGaugh S. S., 2002, *ARA&A*, 40, 263
- Sofue Y., Rubin V., 2001, *ARA&A*, 39, 137
- Springel V., et al., 2005, *Nature*, 435, 629
- Yong D., et al., 2023, *MNRAS*, 526, 2181
- Zwicky F., 1937, *ApJ*, 86, 217
- van Albada T. S., 1968, *BAN*, 20, 47

APPENDIX

A. ECCENTRICITY-DEPENDENT PRIOR ON THE SEMI-MAJOR AXIS

The semi-major axis a of a binary orbit is not directly observable. What is measured is the projected separation r_{\perp} on the sky. To construct a prior on a given the observed r_{\perp} , we compute the expectation value of $\ln(r_{\perp}/a)$ averaged over random orbital phases and viewing angles, following [van Albada \(1968\)](#).

The projected separation of a binary with semi-major axis a and eccentricity e is,

$$r_{\perp} = \frac{a(1-e^2)}{1+e\cos\nu} [1 - \sin^2(\nu + \omega) \sin^2 i]^{1/2} \quad (\text{A1})$$

Here, ν is the true anomaly, ω is the argument of periastron, and i is the inclination. The first factor is the instantaneous three-dimensional separation r . The second factor projects r onto the sky plane.

To obtain $\langle \ln(r_{\perp}/a) \rangle$ at fixed e , we average Equation A1 over the distributions of ν , ω , and i . Because ν appears in both the radial factor and the projection factor, this is simplified by taking the logarithm, which separates the expression into two terms:

$$\left\langle \ln \frac{r_{\perp}}{a} \right\rangle = \int_0^{2\pi} f(\nu) \ln \left(\frac{1-e^2}{1+e\cos\nu} \right) d\nu + \left\langle \frac{1}{2} \ln [1 - \sin^2(\nu + \omega) \sin^2 i] \right\rangle \quad (\text{A2})$$

Here $f(\nu)$ is the time-averaged distribution of the true anomaly for a randomly observed binary,

$$f(\nu) = \frac{(1-e^2)^{3/2}}{2\pi(1+e\cos\nu)^2} \quad (\text{A3})$$

This equation gives more weight to phases near apastron where the binary moves slowly.

We evaluate the first integral by changing variables from ν to the eccentric anomaly E , using the relation

$$\frac{1-e^2}{1+e\cos\nu} = 1 - e\cos E \quad (\text{A4})$$

The mean anomaly $M = E - e\sin E$ is uniformly distributed in $[0, 2\pi)$ for a randomly observed binary, so the frequency distribution of E is

$$\varphi(E) = \frac{1 - e\cos E}{2\pi} \quad (\text{A5})$$

The radial integral becomes

$$\int_0^{2\pi} \frac{1 - e\cos E}{2\pi} \ln(1 - e\cos E) dE = \ln \left(\frac{1 + \sqrt{1-e^2}}{2} \right) + 1 - \sqrt{1-e^2} \quad (\text{A6})$$

The second term in Equation A2 is averaged over ν , ω , and i . For isotropically oriented orbits, the distributions are $h(i) = \sin i$ and $g(\omega) = 1/(2\pi)$. Writing $x = \nu + \omega$, the integral over ω shifts the integration variable but does not change the limits over a full period, so the average of the projection factor does not depend on $f(\nu)$. The remaining integral is

$$\frac{1}{2\pi} \int_0^{2\pi} dx \int_0^1 dt \frac{1}{2} \ln(\cos^2 x + t^2 \sin^2 x) \quad (\text{A7})$$

where $t = \cos i$. Evaluating the inner integral over t and then the outer integral over x gives $\ln 2 - 1$ ([van Albada 1968](#)).

Adding the two terms,

$$\begin{aligned} \left\langle \ln \frac{r_{\perp}}{a} \right\rangle &= \ln \left(\frac{1 + \sqrt{1-e^2}}{2} \right) + 1 - \sqrt{1-e^2} + \ln 2 - 1 \\ &= \ln \left(1 + \sqrt{1-e^2} \right) - \sqrt{1-e^2} \end{aligned} \quad (\text{A8})$$

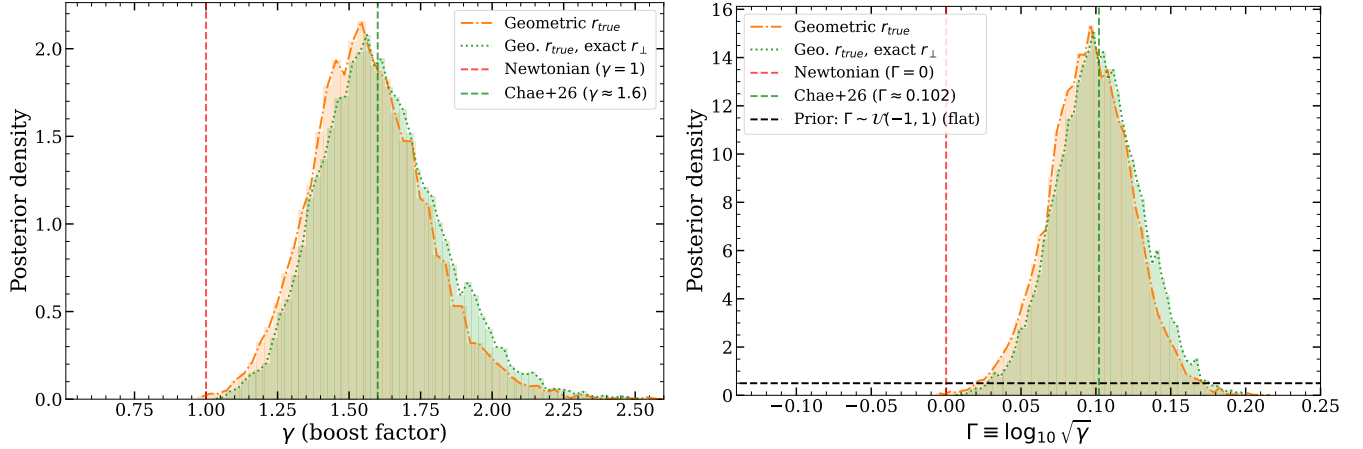


Figure 4. Posterior distributions comparing the effect of treating the projected separation as uncertain versus exact, both using the geometric de-projection for r_{true} (no independent semi-major axis). *Left:* posterior distributions of γ . The orange solid curve shows the geometric de-projection model with r_{\perp} entering the likelihood with Gaussian uncertainty ($\gamma = 1.56$). The green solid curve shows the same model but with r_{\perp} treated as exact ($\gamma = 1.59$). The vertical red dashed line marks the Newtonian prediction ($\gamma = 1$) and the vertical green line shows the result from [Chae et al. \(2026\)](#). *Right:* the same posteriors expressed in terms of $\Gamma \equiv \log_{10} \sqrt{\gamma}$. The horizontal dotted line shows the flat prior $\Gamma \sim \mathcal{U}(-1, 1)$. The two curves are nearly identical, demonstrating that the r_{\perp} treatment has a negligible effect ($\Delta\gamma \approx 0.03$) compared to the semi-major axis parameterization ($\Delta\gamma \approx 0.44$).

This equation now depends only on e .

The ratio a/r_{\perp} decreases with increasing eccentricity because eccentric orbits spend more time near apastron, where the instantaneous separation is already close to a and the projected separation is correspondingly large.

In our model, we use the negative of Equation A8 as the center of the prior on $\eta = \ln(a/r_{\perp})$:

$$\mu_e = \sqrt{1 - e^2} - \ln\left(1 + \sqrt{1 - e^2}\right) \quad (\text{A9})$$

The eccentricity e is drawn from the same separation-dependent prior used for the orbital fit, so μ_e varies from system to system. The prior width $\sigma_a = 0.6$ is broad relative to the range of μ_e (≈ 0.07 to 0.31), so the prior is weakly informative and the data can pull the posterior away from the prior center when the kinematic constraints are strong.

B. EFFECT OF TREATING THE PROJECTED SEPARATION AS EXACT

In the main analysis, our geometric de-projection model includes the projected separation r_{\perp} as an observable in the likelihood with Gaussian uncertainty. The [Chae et al. \(2026\)](#) model instead treats r_{\perp} as a fixed, exact quantity. To assess whether this difference contributes to the discrepancy in the inferred γ , we run an additional model variant that combines the geometric de-projection of r_{true} (no independent semi-major axis) with the removal of the r_{\perp} likelihood term, so that r_{\perp} is treated as exact. This variant is the closest analog to the [Chae et al. \(2026\)](#) approach within our framework.

The geometric de-projection model with r_{\perp} uncertainty yields $\gamma = 1.56$ with a 68% credible interval of $[1.38, 1.77]$. When r_{\perp} is instead treated as exact, the posterior shifts to $\gamma = 1.59$ with a 68% credible interval of $[1.40, 1.82]$. The difference is $\Delta\gamma \approx 0.03$, which is small compared to both the posterior width (~ 0.2) and the shift of $\Delta\gamma \approx 0.44$ caused by replacing the independent semi-major axis with the geometric de-projection. In terms of $\Gamma = \log_{10} \sqrt{\gamma}$, the two variants give $\Gamma = 0.096$ and $\Gamma = 0.101$, respectively.

Figure 4 shows the posterior distributions for both variants in γ (left) and Γ (right). The two posteriors overlap very well, confirming that the treatment of projected separation uncertainty is subdominant. The dominant source of the discrepancy between our baseline result and [Chae et al. \(2026\)](#) is the semi-major axis parameterization, not the handling of r_{\perp} .